A Novel Differential Incoherent Heterodyne Continuous-Wave Radar Receiver Architecture With Increased Phase Sensitivity

Nils C. Albrecht, *Graduate Student Member, IEEE*, Philip Riege, Bartosz Tegowski, Dominik Langer, *Graduate Student Member, IEEE*, and Alexander Koelpin, *Fellow, IEEE*

***Abstract*—This work presents a novel heterodyne radar transceiver architecture based on two separate, incoherent radio frequency (RF) sources. Unlike conventional continuous-wave (CW) radar systems, the proposed approach measures the square of the channel transfer function, resulting in doubled phase sensitivity. This enhancement arises from a differential evaluation of the downconverted intermediate-frequency (IF) signals, which enables precise tracking of phase changes without requiring phase-locked local oscillators. The associated signal-processing and calibration methods are derived, allowing for accurate reconstruction of the dynamic target response, even in the presence of static reflections and without needing knowledge of the calibration target's absolute position. Additionally, the effect of oscillator phase noise is evaluated. Experimental validation using high-precision linear motion confirms that the system accurately tracks target displacement and delivers results comparable to those obtained with a commercial vector network analyzer (VNA). By eliminating the need for RF phase synchronization between transceivers, the architecture significantly reduces hardware complexity and is well-suited for integration and miniaturization. Although demonstrated with a single transceiver pair, the method scales naturally to multichannel configurations, enabling low-complexity multiple-input–multiple-output (MIMO) radar systems with enhanced sensitivity.**

***Index Terms*—Continuous-wave (CW) radar, incoherent radar, interferometric radar, radar, radar modeling, signal processing.**

I. Introduction

CONTINUOUS-WAVE (CW) radars are versatile devices used in various applications, including industrial sensors [1], motion detection, and medical diagnostics [2]. Their straightforward design and high sensitivity make them cost-effective and capable of detecting small movements over long distances [3]. Among the different radar principles, CW systems stand out for their simple architecture, high phase sensitivity, and inherently continuous-time operation. Unlike modulated radar types such as frequency-modulated CW (FMCW), CW systems observe the instantaneous phase and amplitude of the reflected signal. This property enables high temporal resolution and wideband tracking of small-scale motions such as vibrations or structural oscillations, making CW radar particularly attractive for near-field sensing, vital-sign monitoring, and precision displacement measurement.

However, CW systems face several fundamental limitations. The measured phase is ambiguous modulo 2π, restricting the unambiguous range to half a wavelength. Moreover, static targets produce dc voltages at the baseband, which are highly susceptible to temperature drifts and offset errors. These effects severely limit the long-term stability and accuracy of conventional CW systems. This motivates the search for CW radar architectures that retain high phase sensitivity and temporal resolution while mitigating dc-offset-related errors and phase ambiguities.

To address phase imbalance and offset issues, several studies have proposed digital quadrature demodulation schemes based on the Hilbert transform [4], [5], [6]. These methods aim to reconstruct analytic signal representations and digitally recover the in-phase and quadrature components, thereby avoiding analog IQ mixers and reducing hardware complexity. However, their applicability in CW radar is limited. Because real-valued mixing in the analog front end inherently removes negative frequency components, signals centered at dc—such as reflections from static or slowly moving targets—cannot be fully reconstructed digitally. Consequently, while Hilbert transform-based approaches can correct quadrature imbalance, this is only valid if the signal of interest is not frequency-symmetric around dc [7], or if the system employs heterodyne downconversion to a low intermediate frequency (IF) before digitization [4]. Therefore, in conventional homodyne CW radar, these techniques cannot resolve phase ambiguities or eliminate offset-related errors.

An alternative is heterodyne radar, where the received signal is downconverted to a nonzero IF before digitization [8], [9]. Processing at an offset frequency enables filtering of dc offsets without distorting relevant information. However, precise phase recovery requires oscillator coherence [10]. Maintaining such coherence at RF frequencies increases system complexity and limits the spatial separation of transceivers, since synchronization typically relies on shared RF References. To gain spatial information beyond range measurements, multiple-input–multiple-output (MIMO) radars employ several transmit

Received 5 August 2025; revised 30 September 2025; accepted 31 October 2025. This work was supported by the Deutsche Forschungsgemeinschaft (DFG, German Research Foundation)-SFB 1483, EmpkinS under Project ID 442419336. *(Corresponding author: Nils C. Albrecht.)*

The authors are with the Institute of High-Frequency Technology, Hamburg University of Technology, 21073 Hamburg, Germany (e-mail: nils.albrecht@tuhh.de; philip.riege@tuhh.de; bartosz.tegowski@tuhh.de; dominik.langer@tuhh.de; alexander.koelpin@tuhh.de).

Digital Object Identifier 10.1109/TMTT.2025.3633498

and receive channels. These enable beamforming and near-field imaging [11], but demand phase synchronization across all transceivers, which poses significant technical challenges [12], [13]. Solutions include software-based synchronization [14] or phase locking at lower frequencies [15], but both add hardware and calibration overhead.

In related research areas, synchronization between spatially separated radar units is intentionally relaxed. Gottinger et al. [16], for instance, proposed a coherent processing scheme using two full-duplex transceivers that mutually receive each other's signals. Their approach estimates oscillator phase distortions a posteriori, combining both bistatic and monostatic responses to reconstruct coherent measurements. While effective, such systems require bidirectional links and explicit oscillator mismatch estimation. Similar mutual-reception principles are also employed in cooperative MIMO radar networks using highly integrated FMCW sensors [17]. These systems exchange modulated chirp signals and jointly reconstruct spatial information. However, they operate with discrete-time modulation and rely on explicit synchronization or postprocessing alignment to ensure coherence across units.

Conventional interferometric sensor architectures, in turn, employ a dedicated reference path to linearize phase and mitigate quadrature imbalance. Such reference-based interferometers are widely used in both microwave and optical systems to stabilize phase measurements and correct nonidealities [18], [19]. In these systems, a portion of the transmitted signal is guided along a reference branch and combined coherently with the measurement signal, allowing compensation of drift and nonlinearity. However, these architectures inherently require phase coherence between reference and measurement channels, as well as analog combination at RF or optical frequencies, which increases hardware complexity and limits scalability.

Against this background, the method presented in this article introduces a novel heterodyne interferometric concept tailored for unmodulated CW operation. It enables broadband measurement of vibrations and small displacements at close range with high temporal resolution—a regime where FMCW radar is often limited by chirp duration, sampling rate, and bandwidth constraints. The proposed system employs mutual reception between two incoherent transceivers, each operating at slightly offset frequencies. Unlike [16], it omits any monostatic paths and does not rely on posthoc estimation or correction of oscillator phase distortions. The frequency offset defines an IF at which both received signals are synchronously sampled and digitally mixed. By differential digital evaluation, the system yields a response proportional to the square of the radar channel, effectively doubling phase sensitivity per unit distance. Operation at a defined IF suppresses dc drifts and environmental offsets, enabling stable, high-sensitivity phase measurements without RF coherence or complex calibration. This architecture combines the robustness of heterodyne systems with the simplicity of CW radar, while maintaining continuous-time operation ideally suited for vibration analysis, resonance detection, and micromotion tracking. Furthermore, by replacing the coherent reference path with an independent transceiver, the approach achieves similar benefits—such as drift suppression and enhanced phase sensitivity—without analog coherence links, allowing distributed, scalable architectures and simplified hardware implementation.

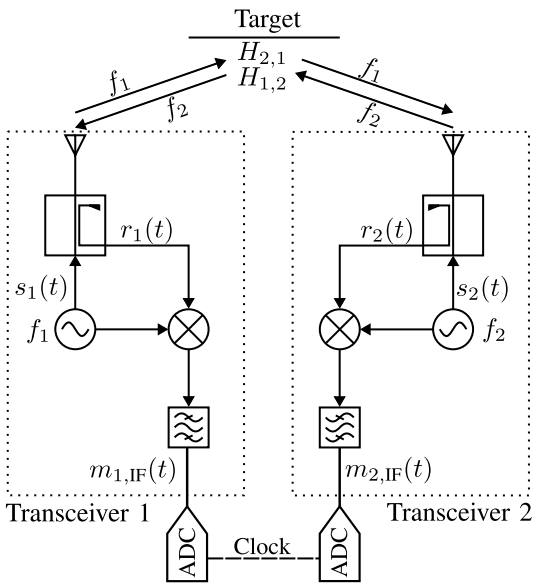

Fig. 1. Block diagram of the proposed transceiver scheme. Individual transceivers 1 and 2 transmit on different frequencies while the resulting IF signals are simultaneously digitized.

The remainder of this article is structured as follows. Section II introduces the general transceiver setup. Section III analyzes the impact of phase noise. Section IV presents the calibration scheme. Section V describes the experimental setup. Section VI discusses the measurement results. Section VIII concludes the article.

II. Architecture Description

Fig. 1 illustrates the proposed transceiver setup. It consists of two independent transceivers, each utilizing a separate local oscillator at a slightly offset frequency. Each transceiver functions as a classic homodyne CW system, utilizing a local oscillator for both transmission and downconversion. The local oscillators are set to slightly different frequencies, f_1 and f_2, related by

$$f_2 = f_1 + f_\Delta \tag{1}$$

where the frequency offset f_Δ satisfies $f_\Delta \ll f_1$. Each transceiver's transmit and receive paths are connected to a single antenna via a directional coupler or circulator. The signal from transceiver 1 is reflected by the target and received by transceiver 2, where it is downconverted to an IF f_Δ by mixing with f_2. Conversely, the signal from transceiver 2 is received and downconverted by transceiver 1.

While RF generation and initial mixing occur in analog hardware, the resulting IF signals are digitized after the mixer and processed digitally. The transmitted signals are defined as

$$s_1(t) = A_1 \cos\left(2\pi f_1 t + \varphi_{0,1}\right) \tag{2}$$

$$s_2(t) = A_2 \cos\left(2\pi f_2 t + \varphi_{0,2}\right) \tag{3}$$

with respective frequencies f_1 and f_2 and initial phases $\varphi_{0,1}$ and $\varphi_{0,2}$.

The transmission channel $H_{i,j}$ between transceivers includes not only the propagation effects between the antennas but also the antenna characteristics themselves. When referenced to the antenna ports, this transmission channel corresponds to the complex scattering parameter between the two antennas and inherently includes gain, mutual coupling, and reflection effects. For the following derivation, the channel is assumed to be static during a single measurement. For a static, reciprocal channel, the phase of the dominant propagation term varies approximately linearly with frequency

$$\varphi(f) \underset{\sim}{\propto} -\,4\pi\frac{fR}{c} \tag{4}$$

for a round-trip path of length $2R$. Hence, the phase change across a small offset f_Δ is

$$\Delta\varphi \;\triangleq\; \varphi(f_1+f_\Delta) - \varphi(f_1) \;\approx\; -\frac{4\pi f_\Delta R}{c}. \tag{5}$$

As a result, with small offsets $f_\Delta \ll f_1$ and short distances, both transceivers experience approximately the same channel response, only differing by a small phase offset. Additionally, under these conditions, the channel is considered reciprocal, thus,

$$H_{2,1} = H_{1,2} = H = |H|e^{j\varphi}. \tag{6}$$

The received real-valued signals are expressed as

$$r_1(t) = A_2\,|H(f_2)|\cos\left(2\pi f_2 t + \varphi_{0,2} + \varphi(f_2)\right) \tag{7}$$

$$r_2(t) = A_1\,|H(f_1)|\cos\left(2\pi f_1 t + \varphi_{0,1} + \varphi(f_1)\right). \tag{8}$$

As only the heterodyne signals are considered, the homodyne components are omitted for clarity. In practice, these are present but will be filtered out in the IF stage and will not be used for ranging. Mixing the transmit and receive signals yields frequency components at the sum ($f_1 + f_2 \approx 2\ f_1$) and difference ($f_\Delta = f_2 - f_1 \ll f_1$) frequencies. The undesired high-frequency component at approximately $2f_1$ is easily removed using a simple bandpass filter, leaving only the desired IF signals

$$m_{1,\mathrm{IF}}(t) = k_1\,|H(f_2)|\cos\left(2\pi f_\Delta t + \Delta\Phi + \varphi(f_2)\right) \tag{9}$$

$$m_{2,\mathrm{IF}}(t) = k_2\,|H(f_1)|\cos\left(2\pi f_\Delta t + \Delta\Phi - \varphi(f_1)\right) \tag{10}$$

where the initial phase difference is defined as $\Delta\Phi = \varphi_{0,2} - \varphi_{0,1}$. The mixing process introduces an additional conversion gain, G_c, which relates the RF input power to the IF output power after the mixer. Even if identical transceivers are used, slight variations between the conversion gains are to be expected. The amplitudes after mixing are, therefore, defined as

$$k_1 = A_2 G_{c1} \tag{11}$$

$$k_2 = A_1 G_{c2}. \tag{12}$$

These IF signals are subsequently digitized for further digital processing.

Since the frequency offset f_Δ is small, the system can, in practice, be oversampled such that the entire band-limited phase-noise spectrum around the carrier is included in the digitized signal. This ensures that the discrete-time representation captures not only the ideal carrier but also its noise skirts. In the present derivation, amplitude and phase noise contributions of the radar front end and the analog-to-digital converter (ADC) are neglected for clarity. For practical implementations, however, the ADC should be chosen such that its noise power spectral density (PSD) is below the noise floor set by the analog front-end components (e.g., LNA and mixer), to avoid degrading the overall system noise performance. Since the sampling rate exceeds the Nyquist rate with a margin, the sampled signal is mathematically equivalent to its continuous-time counterpart, apart from quantization noise. Therefore, the subsequent analysis can be conveniently carried out in continuous-time without loss of generality.

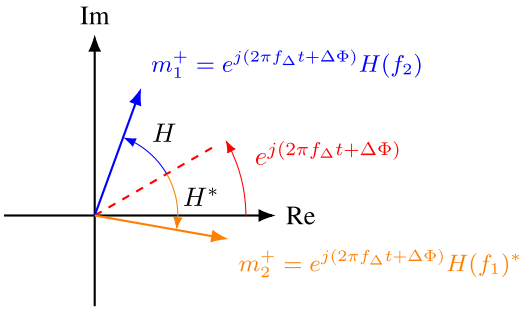

Fig. 2. Pointer diagram of the two analytic receive signals m_1^+ and m_2^+ after the analog mixing process.

Afterward, the signals are converted into analytic signals using the Hilbert transform ($\mathcal{H}$)

$$m_1^+(t) = m_{1,\mathrm{IF}}(t) + j\mathcal{H}\left\{m_{1,\mathrm{IF}}(t)\right\} \tag{13}$$

$$m_2^+(t) = m_{2,\mathrm{IF}}(t) + j\mathcal{H}\left\{m_{2,\mathrm{IF}}(t)\right\}. \tag{14}$$

Using Euler's identity, the analytic signals are expressed as

$$m_1^+(t) = k_1\,|H(f_2)|\,e^{j(2\pi f_\Delta t + \Delta\Phi + \varphi(f_2))} \tag{15}$$

$$m_2^+(t) = k_2\,|H(f_1)|\,e^{j(2\pi f_\Delta t + \Delta\Phi - \varphi(f_1))}. \tag{16}$$

It is worth noting that this approach eliminates the need for analog quadrature demodulation in hardware. In conventional CW radar systems, quadrature mixers are typically required to obtain a complex-valued baseband signal from which the phase can be uniquely determined. In contrast, the real-valued IF signal in this architecture is digitized and converted into an analytic signal using the Hilbert transform. This allows for ideal analytic signal generation in the digital domain (limited only by sampling and quantization), without suffering from typical analog IQ imperfections such as gain and phase imbalance, while still being able to recover the phase information from the signal. From a system perspective, this represents a significant simplification and robustness advantage. From (15) and (16), it is clear that both IF signals share a common phasor rotating at f_Δ, differing only in the complex conjugate of the channel component. This phase relationship is illustrated in Fig. 2.

Since the transceivers are not phase-locked, and $\Delta\Phi$ is, therefore, unknown, the resulting IF signals alone cannot be used for ranging. However, the phase relationship between the signals contains information about the target distance. Through digital mixing of the IF signals, it is possible to extract both

the phase relation of the signal sources and the square of the transmission channel

$$\begin{aligned} M_\Delta(t) &= m_1^+(t) \cdot m_2^+(t) \\ &= k_1 k_2 \left|H(f_2)\right| \left|H(f_1)\right| \cdot e^{j(4\pi f_\Delta t + 2\Delta\Phi + \varphi(f_2) - \varphi(f_1))} \end{aligned} \tag{17}$$

$$\begin{aligned} M_H &= m_1^+(t) \cdot m_2^{+*}(t) \\ &= k_1 k_2 \left|H(f_2)\right| \left|H(f_1)\right| \cdot e^{j(\varphi(f_2) + \varphi(f_1))}. \end{aligned} \tag{18}$$

Using (17), the unknown frequency difference f_Δ may be reconstructed from the two IF signals, assuming a constant, nonzero channel response during the measurement period. For a frequency-flat channel with a dominant target, the phase is locally approximately linear in frequency, such that

$$\arg\left(H(f_1)\,H(f_2)\right) \approx \arg\left(H(f_{\text{mid}})^2\right) \tag{19}$$

with $f_{\text{mid}} = (f_1 + f_2)/2$.

Using a Taylor expansion, one obtains the resulting approximation error

$$\left|\arg\left(\frac{H(f_1)\,H(f_2)}{H^2(f_{\text{mid}})}\right)\right| \;\approx\; \tfrac{1}{4}\left|\varphi''(f_{\text{mid}})\right| f_\Delta^2. \tag{20}$$

The leading approximation error is second order in f_Δ. In free-space propagation, $\varphi(f)$ is exactly linear, so the relation holds exactly. In weakly dispersive channels, the error remains negligible provided f_Δ is well below the coherence bandwidth of the channel.

Therefore, in the following, the frequency dependence in the square of the channel is omitted, yielding

$$M_H = m_1^+(t) \cdot m_2^{+*}(t) = k_1 k_2 \underbrace{|H|^2 \cdot e^{2j\varphi}}_{H^2} \tag{21}$$

with

$$H^2 \triangleq H^2(f_{\text{mid}}) \approx H(f_1)\,H(f_2). \tag{22}$$

In (21), both IF signals are combined to extract relative phase information, which forms the basis of the differential architecture. Rather than relying on absolute phase or time-of-flight measurements from a single transceiver, the system exploits the phase relationship between two independently generated and received signals. The term *differential* refers to this principle: information is extracted not from individual signal paths but from the phase difference between the two transceivers' IF signals. This differential processing not only eliminates the need for phase-locked transceivers but also inherently doubles the phase sensitivity. Since the resulting signal contains the square of the transmission channel, phase changes caused by target displacement appear at twice the rate compared to conventional CW radar systems operating at the same carrier frequency. This enables high-sensitivity displacement and vibration measurements even at lower frequencies. In (21), the oscillator frequency difference f_Δ and the static phase offset $\Delta\Phi$ cancel out, leaving only the square of the transmission channel, scaled by a constant.

This derivation demonstrates that information about an unknown complex propagation channel can be obtained using two uncoupled transceivers. In this context, the term "channel" refers to the complex-valued baseband representation of the signal propagation path, including all effects of free-space transmission, target reflection, antenna coupling, and static environmental reflections. It is this aggregate complex response that is tracked and interpreted in all radar systems.

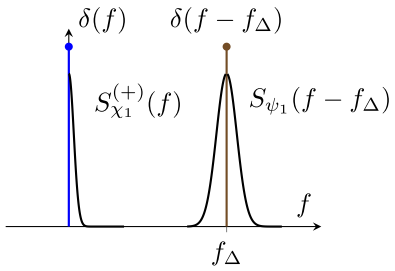

Fig. 3. Schematic one-sided spectrum of $m_1^+(t)$ including phase-noise contributions at the baseband and around f_Δ.

Specifically, the system architecture allows direct access to the squared channel response H^2, which already contains relevant information about the signal path. While the amplitude and phase of H^2 can be used directly to analyze relative changes in the propagation path, this architecture is particularly well-suited for detecting small phase variations caused by target movements, such as vibrations or relative displacements, where relative changes are of primary interest. In such scenarios, absolute range information is not required, and the doubled phase sensitivity provided by H^2 is advantageous. Effectively, the system behaves like a conventional CW radar operating at twice the carrier frequency. If the actual channel response H is required, taking the square root yields

$$\sqrt{M_H} = \pm\frac{\sqrt{k_1 k_2}}{2} H. \tag{23}$$

However, this recovery is ambiguous up to a sign, and this ambiguity cannot be resolved without additional constraints. In practical radar systems, where only relative phase variations are relevant, this ambiguity is often acceptable or can be resolved through temporal phase unwrapping.

III. Phase Noise Analysis

Although in Section II perfect oscillators were assumed, in practice, all oscillators exhibit phase noise, which can degrade system performance. For conventional homodyne CW radars, the so-called range correlation significantly mitigates the impact of phase noise, provided the target distance is sufficiently short [20]. In heterodyne systems, however, the situation is more complex, as phase noise from two independent oscillators contributes to the overall noise. In the simplest nondifferential heterodyne setup, the received signal is first upconverted and then downconverted using two uncorrelated local oscillators. Since their phase fluctuations are statistically independent, no range correlation filtering occurs, and phase noise directly transfers into the baseband signal. Consequently, the impact of oscillator phase noise becomes significantly more pronounced compared to homodyne architectures. In this section, the influence of phase noise on the proposed differential architecture is analyzed. Oscillator phase noise is modeled as a random phase modulation of the ideal carrier. Thus, the transmitter phases become time-varying, $\varphi_{0,1}(t)$

and $\varphi_{0,2}(t)$. Each process is zero-mean and stationary with autocorrelation

$$R_{\varphi_{0,i}}(\tau) = \mathbb{E}\left\{\varphi_{0,i}(t+\tau)\,\varphi_{0,i}(t)\right\}, \quad i \in \{1,2\} \tag{24}$$

where $\mathbb{E}\{\cdot\}$ denotes the expectation operator. The corresponding one-sided power spectral densities (PSDs) are defined as $S_{\varphi_{0,1}}(f) = S_{\varphi_{0,2}}(f) \triangleq S_{\varphi_0}(f)$. Therefore, the signals after the mixer and IF filtering are expressed as

$$m_{1,\mathrm{IF}}(t) = k_1 |H(f_2)| \cos(2\pi f_\Delta t + \psi_1(t) + \varphi(f_2)) \tag{25}$$

$$m_{2,\mathrm{IF}}(t) = k_2 |H(f_1)| \cos(2\pi f_\Delta t - \psi_2(t) - \varphi(f_1)) \tag{26}$$

with

$$\psi_1(t) = \varphi_{0,2}(t-\tau) - \varphi_{0,1}(t) \tag{27}$$

$$\psi_2(t) = \varphi_{0,1}(t-\tau) - \varphi_{0,2}(t) \tag{28}$$

and $\tau = 2R/c$ being the round-trip delay of the signal. Using Bedrosian's theorem [21], the analytic IF signals are approximated as

$$\begin{aligned} m_1^+(t) &\triangleq m_{1,\mathrm{IF}}(t) + j\mathcal{H}\left\{m_{1,\mathrm{IF}}(t)\right\} \\ &\approx k_1 |H(f_2)|\, e^{j(2\pi f_\Delta t + \psi_1(t) + \varphi(f_2))} \end{aligned} \tag{29}$$

$$\begin{aligned} m_2^+(t) &\triangleq m_{2,\mathrm{IF}}(t) + j\mathcal{H}\left\{m_{2,\mathrm{IF}}(t)\right\} \\ &\approx k_2 |H(f_1)|\, e^{j(2\pi f_\Delta t - \psi_2(t) - \varphi(f_1))}. \end{aligned} \tag{30}$$

By employing the Fourier transform of the autocorrelation function, the one-sided PSDs are

$$S_{m_1^+}(f) \approx |k_1|^2 |H(f_2)|^2 \left[\delta(f-f_\Delta) + S_{\psi_1}(f-f_\Delta)\right] \tag{31}$$

$$S_{m_2^+}(f) \approx |k_2|^2 |H(f_1)|^2 \left[\delta(f-f_\Delta) + S_{\psi_2}(f-f_\Delta)\right]. \tag{32}$$

The PSDs of the analytic IF signals in (31) and (32) consist of the carrier at f_Δ and phase-noise contributions around the carrier. As this contribution consists of two uncorrelated noise processes, it is expressed as the sum of their PSDs

$$S_{\psi_1}(f) = S_{\psi_2}(f) = 2\,S_\varphi(f). \tag{33}$$

In addition, both transceivers also exhibit homodyne reception, meaning they receive and downconvert their own transmitted signals. This leads to an additional baseband signal component at dc, which is also affected by phase noise. The PSDs of these baseband components are derived in [20] as

$$S_{\chi_1}(f) = S_{\chi_2}(f) = 4\,\sin^2(\pi f \tau)\,S_\varphi(f) \tag{34}$$

where the sine-squared term arises from the range–correlation filtering effect. A schematic representation of the one-sided spectrum of $m_1^+(t)$ is shown in Fig. 3. Due to the symmetry of the problem, $m_2^+(t)$ has an identical spectrum. The homodyne range–correlation suppresses the baseband phase noise around dc, while the heterodyne phase noise around the carrier is doubled compared to the individual oscillator phase noise. In this derivation, it was assumed that the phase-noise skirt around the carrier is effectively single-sided in the spectrum, which is valid if f_Δ is sufficiently larger than the effective oscillator phase-noise bandwidth. For subsequent processing and estimation of the transmission channel, a bandpass filter around f_Δ is applied. With a correctly chosen filter, the baseband contribution around dc may be neglected while the doubled heterodyne phase noise fully passes. Applying (21) and mixing the two bandpass-filtered analytic signals yields

$$\begin{aligned} M_H(t) &= m_1^+(t)\,\left(m_2^+(t)\right)^* \\ &\approx \left[k_1 |H(f_2)|\, e^{j(2\pi f_\Delta t + \psi_1(t) + \varphi(f_2))}\right] && (35) \\ &\times \left[k_2 |H(f_1)|\, e^{j(2\pi f_\Delta t - \psi_2(t) - \varphi(f_1))}\right]^* && (36) \\ &= k_1 k_2 H^2\, e^{j[\psi_1(t) + \psi_2(t)]} && (37) \end{aligned}$$

with

$$\begin{aligned} \psi_1(t) + \psi_2(t) = \varphi_{0,2}(t-\tau) - \varphi_{0,2}(t) \\ + \varphi_{0,1}(t-\tau) - \varphi_{0,1}(t). \end{aligned} \tag{38}$$

Using the small-angle approximation

$$e^{j(\psi_1+\psi_2)} \approx 1 + j(\psi_1 + \psi_2) \tag{39}$$

the resulting PSD becomes

$$S_{M_H}(f) \approx \left|k_1 k_2 H_c^2\right|^2 \left[\delta(f) + S_{\Sigma\psi}(f)\right], \qquad f \geq 0 \tag{40}$$

where $S_{\Sigma\psi}(f)$ is the PSD of the combined phase noise of both oscillators, each filtered by the range–correlation function [20]. Since the two oscillators are independent, their contributions add up to

$$S_{\Sigma\psi}(f) = 8\,\sin^2(\pi f \tau)\,S_\varphi(f). \tag{41}$$

This has the following implications: For a practical system, the tone spacing f_Δ should be chosen such that it is at least twice the effective phase-noise bandwidth of the oscillators. This ensures that the homodyne (dc-centered) signal components and the desired heterodyne signal do not spectrally overlap. Once this condition is satisfied, further increasing f_Δ does not provide additional benefits, as the phase-noise suppression is determined by the spectral separation rather than the absolute offset. However, larger offsets would unnecessarily increase the required ADC sampling rate and dynamic range.

With sufficient spacing, effective bandpass filtering around f_Δ can be applied, which removes the baseband phase-noise contribution completely. The remaining phase noise around the carrier is doubled compared to the individual oscillator phase noise. When mixing the two bandpass-filtered signals, the resulting phase-noise PSD is shaped by a sine-squared factor, which suppresses low-frequency phase noise. This suppression is most effective for small delays τ, corresponding to short target distances. Therefore, similar to conventional homodyne CW radar systems, the differential heterodyne architecture benefits from range–correlation filtering of low-frequency phase noise, provided that the target distance is sufficiently short.

The residual phase fluctuations can be related to an equivalent range error. In practice, no measurement can observe the instantaneous phase directly, since every radar operates with a finite measurement time. Therefore, the system estimates the phase over a finite observation interval T by averaging the noisy signal. This averaging can be described by applying a rectangular window

$$w_T(t) = \frac{1}{T}\,\mathbf{1}_{[0,T]}(t)$$

which limits the effective measurement bandwidth.

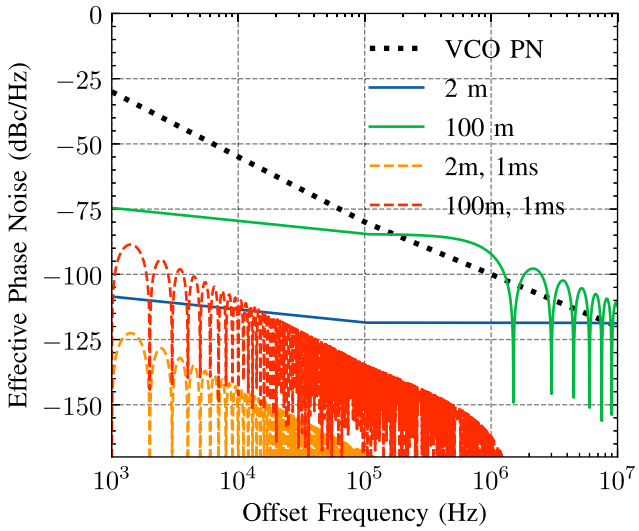

Fig. 4. Effective single-sideband phase-noise spectrum of a low-cost 24-GHz voltage-controlled oscillator (VCO) (*Infineon BGT24LTR11N16*) when used in a differential heterodyne configuration. Solid lines: spatial shaping only; dashed lines: additional temporal averaging with $T = 1$ ms.

In the frequency domain, this window corresponds to a convolution with its Fourier transform

$$W(f) = \operatorname{sinc}(fT) = \frac{\sin(\pi f T)}{\pi f T}.$$

As a result, windowing acts as a low-pass filter on the phase noise, with power response

$$|W(f)|^2 = \operatorname{sinc}^2(fT).$$

The variance of the residual phase error is, therefore, determined by the filtered spectrum $S_{\Sigma\psi}(f)\,|W(f)|^2$. Integrating this spectrum yields the total phase variance after averaging. Finally, the resulting root-mean-square (rms) range error is

$$\sigma_R = \frac{c}{8\pi f_{\mathrm{mid}}} \sqrt{\int_0^\infty 8\,\sin^2(\pi f\tau)\,S_\varphi(f)\,\operatorname{sinc}^2(fT)\,\mathrm{d}f}. \quad (42)$$

As a representative example, the *Infineon BGT24LTR11N16* is considered, a low-cost 24-GHz ISM-band radar transceiver without PLL stabilization and, therefore, exhibiting relatively poor near-carrier phase noise. According to the datasheet, the phase-noise levels are specified as −55 dBc/Hz at a 10 kHz offset and −80 dBc/Hz at 100 kHz. The effective spectra after differential shaping and temporal averaging are shown in Fig. 4. For a target at $R = 2$ m and an integration time of $T = 1$ ms, the $\sin^2(\pi f\tau)$ factor strongly suppresses low-frequency noise, resulting in a residual range error of approximately 0.03 μm. At $R = 100$ m, this suppression effect diminishes, and the same oscillator produces an error of about 1.5 μm. Without temporal averaging, the residual error increases to roughly 5 μm at 2 m and 75 μm at 100 m. These results demonstrate that short-range operation benefits significantly from range correlation filtering, whereas at larger ranges, the oscillator phase-noise floor ultimately limits the achievable precision. Consequently, even for a low-cost oscillator, phase-noise-induced range fluctuations remain negligible at short distances.

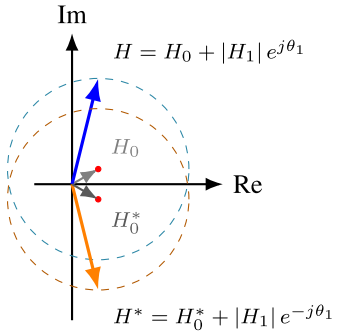

Fig. 5. Pointer diagram of the two analytic receive signals after the analog mixing process with a static channel including a target-independent static cross-coupling contribution. The blue vector represents the signal from transceiver 1, while the orange vector represents the signal from transceiver 2. The gray vector represents the static channel component H_0. The dashed circles represent the trajectories of the complex signals in the complex plane, which are centered around H_0 and H_0^*.

IV. Calibration

While it is possible to obtain H^2 directly, and therefore $2\arg H$, from (21), a calibration may be necessary in a practical system to isolate the target-related channel contribution from direct antenna coupling and other reflections within the setup. For a conventional homodyne CW radar, this can be easily solved by subtracting a constant offset from the measured complex signal. However, due to the nonlinear behavior of the heterodyne system, additional processing is required. Consider a system in which the transmission channel is given by $H = H_0 + H_1$, consisting of a constant component H_0, arising from direct coupling between the antennas, and a target component H_1, which is to be measured accurately. The effects of phase noise can be neglected in this case, as they do not create a systematic offset on the signals. The resulting analytic baseband signals are given by

$$m_1^+(t) = \frac{k_1}{2} \cdot e^{j(2\pi f_\Delta t + \Delta\Phi)} \underbrace{(H_0 + H_1)}_{H} \quad (43)$$

$$m_2^+(t) = \frac{k_2}{2} \cdot e^{j(2\pi f_\Delta t + \Delta\Phi)} \underbrace{(H_0 + H_1)^*}_{H^*}. \quad (44)$$

It is assumed that $H_0 = |H_0|e^{j\theta_0}$ is static; in contrast, $H_1 = |H_1|e^{j\theta_1(x)}$ varies with the target distance through $\theta_1(x)$. The baseband signals trace the complex trajectories depicted in Fig. 5. Note that the rotation due to the common difference frequency is omitted, as both vectors rotate synchronously around the origin. Only their relative differences are of interest. As the target moves and, therefore, changes the argument of the channel, the baseband signals will rotate in opposite directions, resulting in increased phase sensitivity concerning their phase difference. The amplitude of the target's reflection $|H_1|$ is assumed to be constant, an assumption that holds for small target displacements relative to the overall distance. The square of the channel can be extracted using (21)

$$M_H = \frac{k_1 k_2}{4} \cdot \underbrace{|H_0 + H_1|^2 \cdot e^{2j\arg(H_0 + H_1)}}_{H^2}. \quad (45)$$

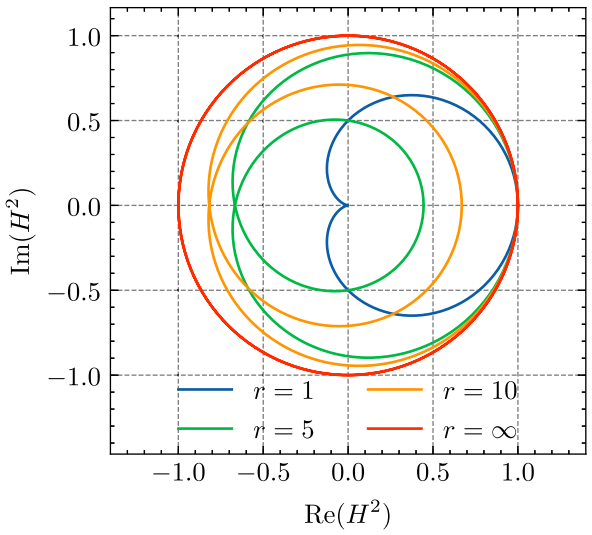

Fig. 6. Exemplary normalized complex trajectories of H^2 for different values of r. For large values of r, the trajectory is close to a circle, while for small values of r, the trajectory becomes more complex and self-intersecting.

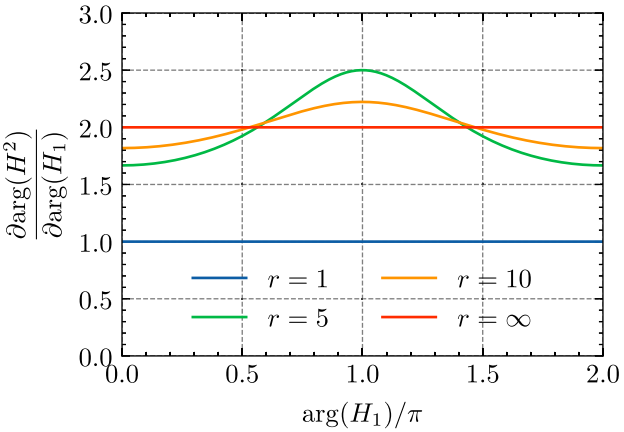

Fig. 7. Phase sensitivity $\partial\ \arg(H^2)/\partial\ \arg(H_1)$ of the radar system for different values of r.

Using $r = (|H_1|)/(|H_0|)$ and $\theta' := \theta_1 - \theta_0$, H may be rewritten to

$$H = H_0\left(1 + re^{j\theta'}\right). \tag{46}$$

Therefore,

$$H^2 = H_0^2\left(1 + 2re^{j\theta'} + r^2e^{j2\theta'}\right). \tag{47}$$

Fig. 6 exemplarily presents complex trajectories of H^2 for different values of r. It can be observed that these trajectories deviate from their ideal circular form, instead forming self-intersecting shapes. In Fig. 7, the phase sensitivity $\partial\ \arg(H^2)/\partial\ \arg(H_1)$ is shown for these cases. In the ideal case $r \to \infty$, a constant value of two indicates a doubled sensitivity. However, for finite offsets, the resulting phase sensitivity varies significantly. Since the measured phase of H^2 is not a linear function of the phase change introduced by the target (e.g., due to displacement), it becomes difficult to relate phase variations to absolute changes in range directly. The system does not exhibit a uniform scaling between path length changes and phase changes. This nonlinearity complicates distance tracking, especially if high precision is required over larger ranges. Therefore, maintaining a constant phase sensitivity is desirable for most applications.

To compensate for this sensitivity distortion, the goal is to extract the target component H_1, which carries the desired dynamic information, from the total measured signal $H = H_0 + H_1$. This requires identifying the static component H_0, as it is responsible for the deviation from ideal circular phase trajectories and the loss of constant phase sensitivity.

The shapes depicted in Fig. 6 can be recognized as a linearly affine-transformed limaçon in the complex plane [22]. This type of curve is well understood mathematically and can be used to derive an implicit expression for the distorted radar response. The general form of a limaçon is given by [22]

$$z(\kappa) = \frac{a}{2} + be^{j\kappa} + \frac{a}{2}e^{j2\kappa} \tag{48}$$

in the complex plane. With

$$p = \mathrm{Re}\{z\} = (b + a\cos\kappa)\cos\kappa \tag{49}$$

$$q = \mathrm{Im}\{z\} = (b + a\cos\kappa)\sin\kappa \tag{50}$$

as a direct Cartesian form. An implicit equation for this shape is known from [23]

$$\left(p^2 + q^2 - ap\right)^2 = b^2\left(p^2 + q^2\right). \tag{51}$$

By exploiting the similarity of (47) and (48), it is possible to express the measured signal in a similar form. Substituting $z'(\kappa) = z(\kappa) + 1 - a/2$

$$z'(\kappa) = 1 + be^{j\kappa} + \frac{a}{2}e^{j2\kappa} \tag{52}$$

a shifted limaçon is obtained, which is equivalent to the Cartesian substitution

$$p' = p + 1 - \frac{a}{2} \tag{53}$$

$$q' = q. \tag{54}$$

The measured signal (47) can be expressed as a rotated version of the shifted limaçon (52)

$$\left(H_0^2\right)^{-1} H^2 = z'\left(\theta'\right) \tag{55}$$

with $b = 2r$ and $a = 2r^2$. In Cartesian form, this can be expressed as

$$\frac{1}{|H_0|^2}\begin{bmatrix}\cos(2\theta_0) & \sin(2\theta_0)\\ -\sin(2\theta_0) & \cos(2\theta_0)\end{bmatrix}\begin{pmatrix}u\\ v\end{pmatrix} = \begin{pmatrix}p + 1 - r^2\\ q\end{pmatrix} \tag{56}$$

with $u = \mathrm{Re}\{H^2\}$ and $v = \mathrm{Im}\{H^2\}$ being the Cartesian representation of H^2. Solving for p and q

$$p = \frac{1}{|H_0|^2}\{u\cos(2\theta_0) + v\sin(2\theta_0)\} - 1 + r^2 \tag{57}$$

$$q = \frac{1}{|H_0|^2}\{-u\sin(2\theta_0) + v\cos(2\theta_0)\}. \tag{58}$$

These expressions map the observed signal $H^2 = u + \mathrm{j}v$ to the modified limaçon coordinates in the complex plane. Inserting these into (51) yields the following expression:

$$0 = r^8 - 4r^6 + 6r^4 - 4r^2 + 1$$

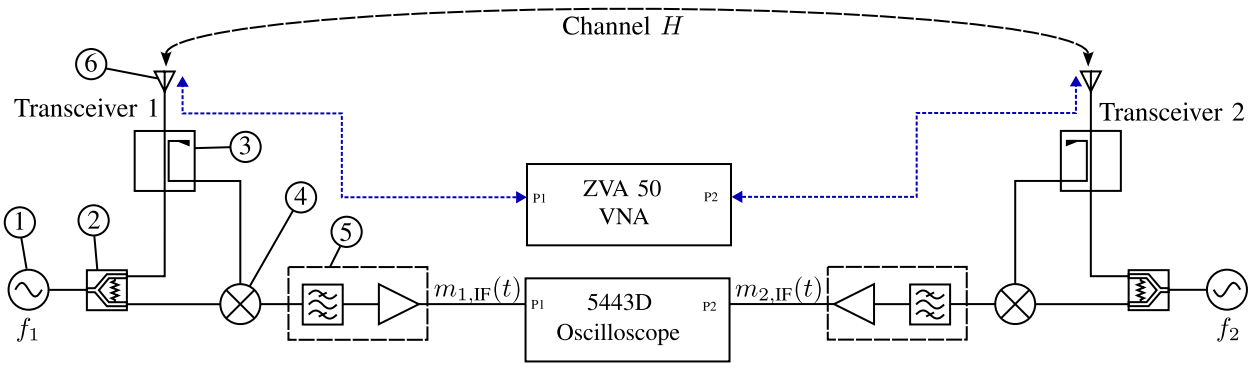

Fig. 8. Block diagram of the measurement setup: Each of the transceivers consists of ① a signal generator, ② 3-dB splitter, ③ directional coupler, ④ fundamental mixer, ⑤ IF amplifier with integrated bandpass filter, and ⑥ antenna. A digital oscilloscope simultaneously samples the IF signals. Additionally, a commercial VNA can be connected to the same set of antennas to serve as a reference.

$$
\begin{aligned}
&- \frac{4r^4}{|H_0|^2}\left(u\cos 2\theta_0 + v\sin 2\theta_0\right) \\
&+ \frac{8r^2}{|H_0|^2}\left(u\cos 2\theta_0 + v\sin 2\theta_0\right) \\
&- \frac{4}{|H_0|^2}\left(u\cos 2\theta_0 + v\sin 2\theta_0\right) \\
&- \frac{2r^4}{|H_0|^4}\left(u^2+v^2\right) - \frac{4r^2}{|H_0|^4}\left(u^2+v^2\right) \\
&+ \frac{4}{|H_0|^4} \\
&\left(u^2\cos^2 2\theta_0 + 2uv\sin 2\theta_0\cos 2\theta_0 + v^2\sin^2 2\theta_0\right) \\
&+ \frac{2}{|H_0|^4}\left(u^2+v^2\right) \\
&- \frac{4}{|H_0|^6}\left(u^3\cos 2\theta_0 + u^2 v\sin 2\theta_0 \right. \\
&\qquad \left. + uv^2\cos 2\theta_0 + v^3\sin 2\theta_0\right) \\
&+ \frac{1}{|H_0|^8}\left(u^4 + 2u^2v^2 + v^4\right). \qquad (59)
\end{aligned}
$$

This equation describes the trajectory of H^2 solely in terms of model parameters, notably incorporating the static channel component H_0 and the dynamic part $H_1(x)$.

The goal of the calibration is to determine the static channel contribution H_0, which distorts the ideal circular phase trajectory. During calibration, a target is moved to induce variations in $H_1(x)$, for example, by translating it over a short range. Importantly, due to the implicit formulation, the exact distance of the target at each point does not need to be known.

The measured signal $H^2(x)$ then traces a distorted trajectory in the complex plane. By fitting (59) to this observed trajectory, the unknown parameter H_0 can be extracted. This fitting process effectively minimizes the discrepancy between the measured H^2 samples and the analytical model, treating H_0 and r as free variables.

Once H_0 has been identified, it can be used to correct subsequent measurements and to recover the channel response associated with the target motion

$$H_1^2 = H^2 + H_0^2 \pm 2H_0\sqrt{H^2}. \qquad (60)$$

As the argument of H_0 only appears with a factor of two within 2π-periodic trigonometric functions in (59), the sign of the resulting H_0 is inherently ambiguous. This ambiguity arises, as described in Section II, because squaring the transfer function introduces a π-angle ambiguity. However, only one of these solutions is physically meaningful and leads to a constant target amplitude. The correct solution can be determined by evaluating the amplitude of H_1^2, which should remain constant over the calibration range. If the amplitude varies significantly, it indicates that the wrong sign was chosen.

This calibration approach assumes a single moving target and a static environment. In more complex scenarios with multiple reflections or moving objects, it is not applicable, and nonlinear distortions will remain. However, for many practical applications, such as precision displacement measurements or vibration sensing in controlled environments, having a single dominant target is a reasonable assumption. The calibration can be performed once during setup or periodically to account for slow changes in the environment.

V. Measurement Setup

The proposed radar architecture is constructed using connectorized laboratory components to validate its measurement performance. An overview of the setup is shown in Fig. 8, while Fig. 9 illustrates its practical implementation. Each transceiver is built from an *Anritsu MG3694B* signal generator ① providing carrier frequencies of f_1 = 19.9995 GHz and f_2 = 20.0005 GHz, resulting in an IF of f_Δ = 1 MHz. The transmit signal is split using a *Marki Microwave PD0140* power divider ②, where one path is fed to a *Krytar 2610* directional coupler ③ and radiated via a *Narda Model 638* horn antenna ⑥ with a gain of 15.4 dBi. The second path serves as the local oscillator input for a *Marki Microwave M40150LKV* fundamental mixer ④. The received signal from the antenna is routed back through the coupler to the mixer and downconverted to IF. This signal is then amplified using a *Mini-Circuits ZKL-1R5* + amplifier ⑥ which also acts as a bandpass filter due to its limited frequency range of 1 MHz to 1.5 GHz. It is subsequently digitized by a *Pico Technology PicoScope 5442D MSO*, which records both IF channels simultaneously at 15 625 ks s^{-1} for 1 56 250 samples

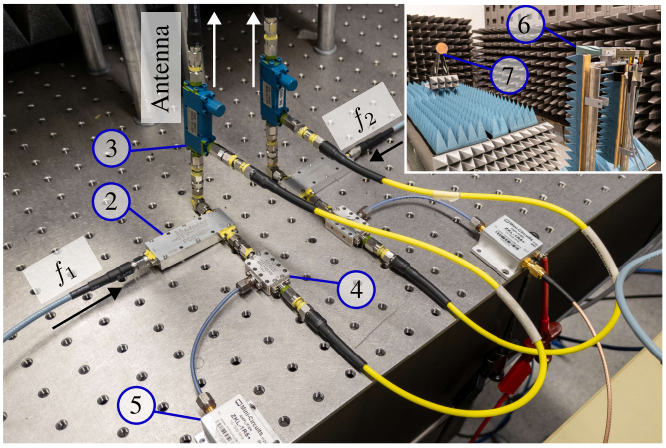

Fig. 9. Measurement setup as presented in Fig. 8. Both transceivers are equally constructed from connectorized laboratory equipment. The LO signals are generated by two independent signal generators outside the frame. The reference target ⑦ on the linear test platform is depicted in the top right corner.

per measurement point, corresponding to a time window of 100 ms. Further signal processing is performed in *Python*.

In addition, a *Rohde & Schwarz ZVA50* vector network analyzer (VNA) is used to provide a reference measurement. The identical horn antennas are connected to the VNA, and the two ports are short–open–load–through (SOLT) calibrated at the coaxial connector reference plane. The VNA records the transmission between both antennas as scattering parameters. As the channel is entirely passive and reciprocal, measuring only one of the transmission paths is sufficient. The measurement bandwidth is set to 100 Hz, while the center frequency is set to 20 GHz.

A precision linear stage equipped with air bearings and a linear motor (*Physik Instrumente A123*) is placed in front of the radar system. This setup allows the target to be moved with a repeatability of 2 μm and a positioning uncertainty of 10 μm over the range of travel. The target is chosen to be a 50-mm copper disk with significantly larger distance than diameter to minimize near-field effects of the target [24], such that the disk can be approximated as a point target.

The two antennas are aligned with the linear stage, so that the target is centered between them and moves perpendicular to the baseline. The linear stage moves in steps of 10 μm over a distance of $\delta x = 6$ cm, which corresponds to approximately four wavelengths at the center frequency of 20 GHz. The initial distance is set to $x_0 = 50$ cm. After the measurements with the incoherent heterodyne system, the horn antennas are reconnected to the VNA, and the measurement is repeated using the same mechanical configuration.

VI. Results

Fig. 10(a) shows the PSD of both IF signals. These predominantly contain the desired difference frequency of 1 MHz, along with some random and shaped low-frequency noise. The broadband noise is attributed to the digital storage oscilloscope.

A fast Fourier transform (FFT)-based brick-wall filter is employed to isolate the desired IF component at 1 MHz while

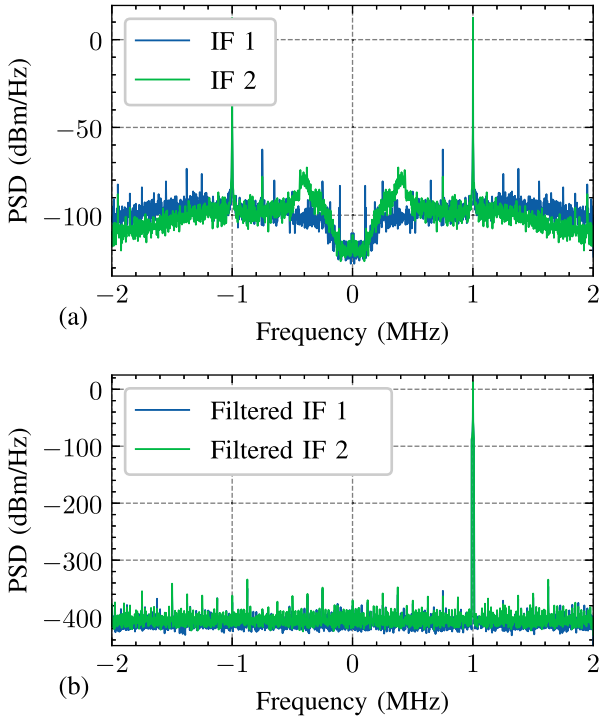

Fig. 10. Measured PSD of (a) IF signals after the digitization process and (b) subsequent filtering steps, removing out-of-band noise and negative frequency components.

simultaneously performing a Hilbert transformation. The time-domain samples are first windowed using a Hamming window and then transformed into the frequency domain via an FFT. Frequencies outside the desired passband are set to zero, after which an inverse FFT is applied to obtain the analytic signal in the time domain.

The signal generators used in this setup exhibit exceptionally low phase noise. With a tone separation of only 1 MHz, the criterion defined in Section III is easily satisfied. The filter bandwidth is set to 100 kHz, thereby covering the relevant phase-noise components of the signal generators down to approximately -100 dBc/Hz.

Fig. 10(b) shows the PSDs after filtering. The broadband noise level is reduced by approximately 300 dB through filtering, limited only by the numerical precision of the double-precision floating-point representation. Compared to analog methods, this digital filtering can be considered ideal. After filtering, the resulting PSD is no longer symmetric, as the Hilbert transform removes all negative frequency components. The power level of the IF signals differs by 2.3 dB, which stems from the tolerances of the analog hardware. However, it is not relevant for the operation of the proposed radar architecture as it only affects the amplitude of the resulting trajectory, but not its shape. Using the signal-processing steps described in Section II, the transfer function between the two antennas is estimated for each measurement location. The resulting measurement points are created within the same 100-Hz bandwidth limit to achieve results comparable to those of the commercial VNA.

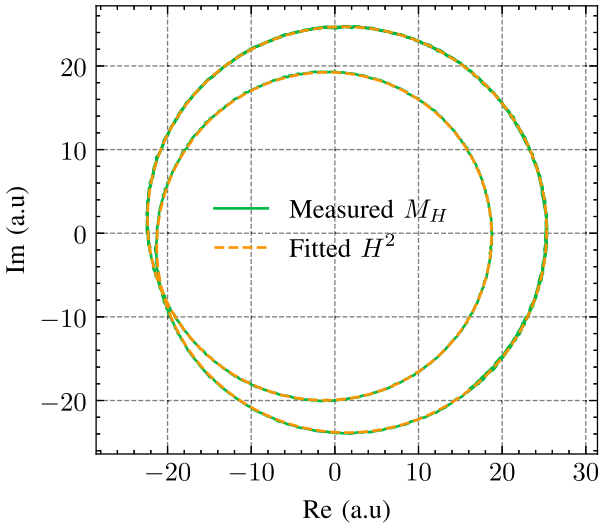

Fig. 11. Raw complex data for $M_H(t)$ from the measurements. Impairments from static reflections and direct antenna coupling are visible as distortions from the ideal circular trajectory. Additionally, H^2 is calculated using the fit parameters from calibration. Both curves show excellent agreement, indicating that the calibration approach is successful.

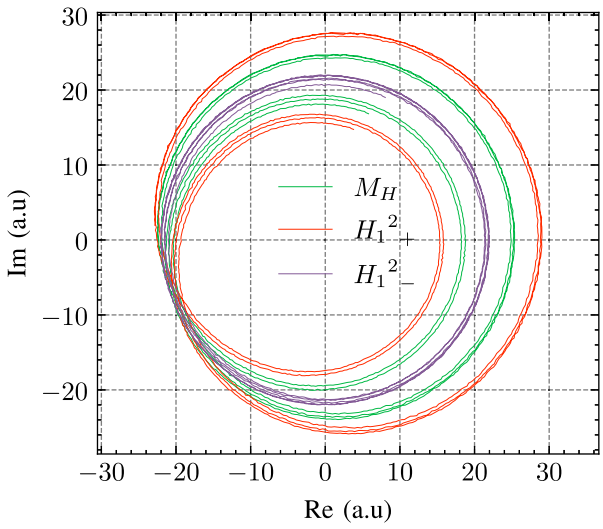

Fig. 12. Measured complex data of H^2 and corresponding results for H_1^2 after calibration. The two possible solutions are shown, with only one being physically meaningful.

Fig. 11 shows the raw complex data of the product $M_H(t)$ obtained from the measurements. In the ideal case of zero cross-coupling, this representation would result in a perfect circle. However, due to static reflections and direct antenna coupling, the data deviates from this ideal trajectory, resulting in a limaçon shape. This distortion is caused by static offsets present in the system, not due to transceiver impairments. Using the calibration approach proposed in Section IV, these static offsets can be removed from the measurement data. In the following, the amplitude term k_1k_2 in (45) is normalized to one, such that $M_H(t) = H^2$. The product of the transceiver gains is, therefore, incorporated into the transmission channel, denoted as H. As only relative changes in the channel are considered in this work, the absolute amplitude of the channel is not a relevant factor. However, using an additional calibration step, the absolute amplitude can be determined, for example, by measuring a known target with a known radar cross section (RCS).

The measurement data are fit to (59) to estimate the parameters of the static coupling using a limited-memory Broyden–Fletcher–Goldfarb–Shanno (L-BFGS) optimization algorithm [25]. As the fit function is highly nonlinear, constraints and an initial guess need to be chosen carefully to ensure a physically meaningful solution.

1) $r \in [1, 20]$: This range restricts the coupling ratio to realistic physical values. A value of $r = 0$ would lead to an infinite ratio of cross-coupling to the reflected path, causing numerical issues, while at $r = 20$ the reflected path is already 20 times stronger than the antenna coupling. Since the horn antennas are facing in the same direction, low but measurable cross-coupling is expected.
2) $\theta_0 \in [0, \pi]$: This accounts for the symmetry of the problem, as shifting θ_0 by π does not change the resulting trajectory.
3) $|H_0| \in [0.1, 10]$: This avoids degenerate solutions by eliminating unrealistically small or large absolute values. The range is chosen in accordance with the overall signal amplitude. The cross-coupling is significantly smaller than the direct signal, making 10 a reasonable upper bound.

The initial guess ($r = 20$, $\theta_0 = 0$, $|H_0| = 0.1$) was deliberately placed at the boundary of the allowed ranges. This guarantees that the optimizer starts in a physically valid region, while still allowing convergence toward the experimentally observed optimum. Such a choice also helps avoid initialization near unphysical or singular values that might prevent convergence. The optimization is performed using the *scipy* library in *Python*, which provides a robust implementation of the L-BFGS algorithm. L-BFGS was selected because it converges faster than first-order methods (such as gradient descent) for smooth problems, and because the implementation allows box constraints, which are convenient for enforcing physically meaningful parameter ranges. In principle, any nonlinear optimization method could be used in this calibration step. The optimization converges to a low residual error after a few iterations, indicating a successful fit and well-estimated parameters. The resulting parameters are $r = 13.13$, $\theta_0 = 0.167$, and $|H_0| = 0.356$. θ_0 is ambiguous in the sense that it can be shifted by π without changing the resulting trajectory. Using these parameters, H^2 is computed for varying θ_1 and plotted in Fig. 11 as a dashed orange line. The excellent agreement between the measured data and the fit function confirms the calibration approach.

Using (60), the calibration can be applied such that only H_1^2 remains in the measurement data. Due to the ambiguity, two possible solutions arise, both of which are plotted in Fig. 12. While one solution results in a perfect circle, the other is

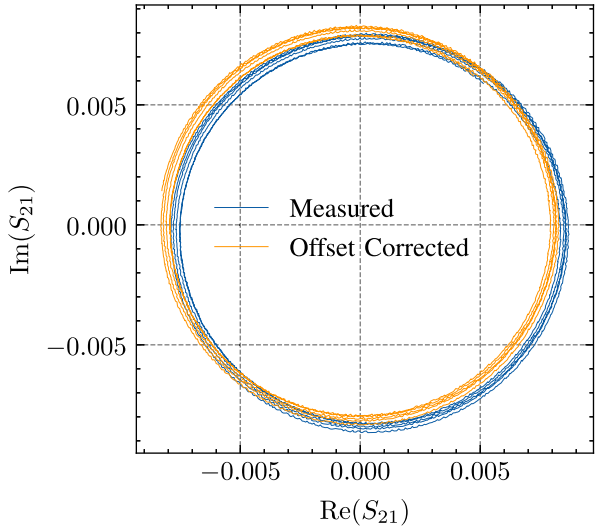

Fig. 13. Calculated channel responses from reference VNA. The blue trace shows raw, uncorrected data, while the result after offset correction is displayed in orange.

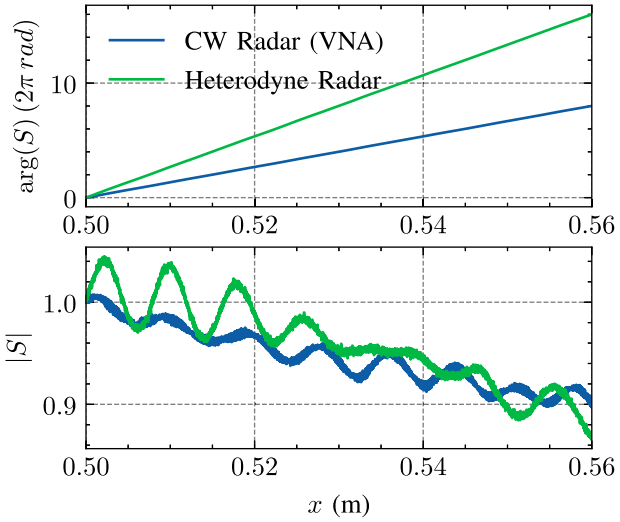

Fig. 14. Measured relative complex channel transfer functions displayed in terms of phase (top) and normalized amplitude (bottom) after offset correction. The phase is shown in full phase rotations per tick.

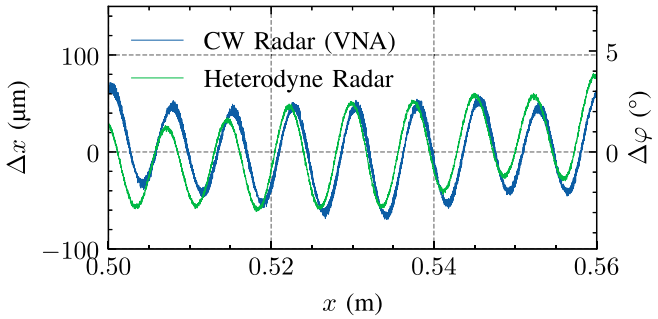

Fig. 15. Positional error between the ground-truth target position x and the position calculated from the argument of the channel response for both systems. The right axis indicates the equivalent phase deviation $\Delta\varphi$.

severely distorted. The solution $H_{1+}^2 = H^2 + H_0^2 + 2H_0\sqrt{H^2}$ is identified as the correct one, since it is the only physically meaningful result under the assumption of a constant target RCS.

Fig. 13 presents the channel measurements in the complex plane for the reference VNA, shown in blue. The system exhibits minimal impairments, and the linearly moving target appears as a circular trajectory in the complex plane. As with the radar data, a calibration step is necessary to remove static reflections from the reference measurement. An ellipse fitting algorithm is employed to eliminate these static reflections, as proposed in [26]. Due to the high quality of the VNA receiver, the resulting signal is not significantly affected by hardware gain or phase imbalances; thus, the ellipse fitting can be simplified to a circular fitting procedure. The calculated center position of the circle is subsequently subtracted from the measurement data.

Similar to the heterodyne radar system, the effects of multipath propagation and self-RCS, as described in [27], are neglected for calibration purposes.

Fig. 14 presents the unwrapped argument and normalized magnitude of the measured transfer functions over distance, after their respective calibrations. For both systems, the complex measurand is normalized to a reference point x_0, reflecting the fact that CW radar systems are typically used for relative measurements

$$S_{\text{vna}}(x) = \frac{S_{21}(x)}{S_{21}(x_0)} \tag{61}$$

$$S_{\text{het}}(x) = \frac{H_1^2(x)}{H_1^2(x_0)} \tag{62}$$

where $S_{21}(x)$ is the complex calibrated transmission coefficient measured by the VNA, and $H_1^2(x)$ is obtained from the heterodyne radar after calibration using (60).

With this consistent normalization, the two systems can be directly compared in both magnitude and phase. The amplitude responses are in good agreement and show the same underlying trend and periodic ripple, which is likely caused by multipath propagation in the measurement environment [28]. Slight differences may be caused by calibration errors. The phase of the heterodyne radar signal changes at twice the rate of that observed in a conventional homodyne CW radar, reflecting the fact that the proposed system measures the square of the channel transfer function. This doubled sensitivity becomes immediately apparent in the normalized representation and is an intrinsic property of the proposed heterodyne architecture. The comparison in Fig. 14 employs a VNA-based homodyne CW setup, serving as a high-fidelity reference for conventional architectures.

Under far-field conditions for both the antennas and the radar target, the phase of the channel transfer function is directly proportional to the target distance

$$\arg\left(S_{\text{vna}}(x)\right) = -2\text{kx} \tag{63}$$

$$\arg\left(S_{\text{het}}(x)\right) = -4\text{kx} \tag{64}$$

where k is the free-space wavenumber at f_{mid} and x the target distance. This allows us to derive the effective distance error

between the measured and actual target positions

$$\Delta x_{\mathrm{vna}}(x) = x - \frac{\arg\left(S_{\mathrm{vna}}(x)\right)}{-2k} \tag{65}$$

$$\Delta x_{\mathrm{het}}(x) = x - \frac{\arg\left(S_{\mathrm{het}}(x)\right)}{-4k}. \tag{66}$$

Fig. 15 presents the error Δx between the measured and expected distances, normalized to zero mean, for both the heterodyne transceiver and the reference measurements from the VNA. The most prominent deviations exhibit a periodicity of half a wavelength and appear similarly in both systems. These deviations stem from multiple reflections between antennas and target [27], [28] and are, therefore, not artifacts of the measurement hardware, but rather real modulations of the transmission channel. A comparison of the relative displacement errors between both instruments shows deviations of less than 20 μm.

VII. Discussion

The VNA-based homodyne CW setup represents a high-performance reference implementation of conventional architectures. Achieving comparable accuracy with two incoherent transceivers, therefore, underscores the effectiveness of the proposed approach. While systematic deviations due to multipath propagation are more pronounced than the differences between the two systems, minor residual discrepancies remain. In both analyses, it is assumed that the target's RCS is constant and that antenna reflections are independent of the connected system. However, neither the horn antennas nor the transceivers are perfectly matched, resulting in internal reflections that are not accounted for in the processing. These likely contribute to the observed residuals. Furthermore, all target positions were recorded sequentially over a period of approximately 60 min, making it difficult to guarantee a constant ambient temperature. Thermal effects are not considered; however, since positional deviations of 20 μm correspond to phase errors of less than one degree, temperature-induced asymmetries in the transceivers are plausible.

In addition to these systematic effects, random errors caused by oscillator phase noise have also been analyzed. Based on the measured phase-noise spectra and the theoretical derivation in Section III, the resulting displacement uncertainty is several orders of magnitude smaller than the systematic deviations observed here. Consequently, the residual errors are dominated by setup-related effects rather than stochastic phase fluctuations, confirming that oscillator phase noise does not limit the achievable accuracy under the given conditions.

It should be emphasized that the applied calibration approach assumes a single dominant target in an otherwise static environment. This simplification is well justified for many CW radar applications, where typically only one primary reflector is present or the antenna gain is sufficiently high to suppress unwanted echoes. In scenarios that deviate from these assumptions—such as environments with multiple targets, significant multipath contributions, or antennas with lower directivity—larger errors may occur. These limitations are comparable to those inherent in conventional CW radar systems employing arctangent-based demodulation, where the same assumption is implicitly applied. For applications that require explicit target separation, as commonly addressed using FMCW radar techniques, additional processing or more advanced signal models would be necessary to achieve comparable accuracy.

These results demonstrate that the proposed heterodyne radar architecture enables measurement of target displacement with twice the phase sensitivity compared to a conventional homodyne CW radar operating at the same carrier frequency. This enhanced sensitivity can be directly exploited for high-resolution applications such as vibration analysis, structural monitoring, or noncontact displacement sensing. In terms of position accuracy, the achieved results closely match those obtained from a calibrated VNA, validating the theoretical predictions.

It should be noted that the laboratory setup was deliberately designed to be highly idealized, with minimal hardware imperfections. The use of low-phase-noise RF signal generators and connectorized components ensures good symmetry and stable coupling conditions between the two transceiver channels. Despite this optimized configuration, residual systematic deviations remain due to reflections in the measurement chain. The channels also exhibit significant gain imbalance; however, as follows from the derivation and confirmed by the measurements, this does not affect the displacement estimation, and no individual calibration of the transceivers is required.

In embedded implementations, additional challenges arise: limited space and power budgets make achieving good isolation and high-quality local oscillators more difficult. Furthermore, the required IF bandwidth is determined by both the target motion and the phase noise of the oscillators. In such systems, minimizing the IF bandwidth is beneficial for reducing power consumption and computational complexity.

The conceptual advantage of the proposed method is the shift from local oscillator coherence to baseband coherence for the transceivers. This significantly simplifies the hardware setup, as IF signals operate at much lower frequencies. Notably, this also enables further extensions. Instead of two transceivers, any number of channels can be used, as long as their carrier frequencies are sufficiently separated. Due to their differing IF frequencies, the individual signal contributions can be extracted simultaneously. This allows for extending the heterodyne concept from single-input–single-output (SISO) systems to MIMO configurations with minimum additional hardware complexity. Coherence between the transceivers is not required; only the respective transceiver frequencies need to be sufficiently spaced, and the IF signals must be simultaneously sampled.

VIII. Conclusion

This work presented a novel heterodyne radar architecture based on differential signal processing between two incoherent transceivers. The core concept enables phase-sensitive channel measurements without requiring oscillator synchronization, while inherently achieving twice the phase sensitivity compared to conventional homodyne CW radar systems. This enhanced sensitivity can be exploited for precise displacement and vibration measurements at the same carrier frequency.

To validate this architecture, a practical implementation using a pair of incoherent laboratory transceivers was constructed. The underlying signal model was derived in detail, and a calibration method was introduced that compensates for static channel components using an implicit expression of the measured signal trajectory. The calibration routine does not require knowledge of the exact position of the target during calibration.

The proposed concept was experimentally validated using a moving radar target. The results demonstrate excellent agreement with reference measurements obtained from a calibrated VNA, confirming both the accuracy and robustness of the approach. While the demonstrated setup is based on laboratory equipment, the method is inherently well-suited for integration and miniaturization, as it avoids the technically demanding requirement of local oscillator coherence. The architecture thus offers a scalable and hardware-efficient solution for implementing high-sensitivity radar systems.

REFERENCES

[1] S. Mann et al., "High-precision interferometric radar for sheet thickness monitoring," *IEEE Trans. Microw. Theory Techn.*, vol. 66, no. 6, pp. 3153–3166, Jun. 2018.

[2] N. C. Albrecht et al., "EmRad: Ubiquitous vital sign sensing using compact continuous-wave radars," *IEEE Open J. Eng. Med. Biol.*, vol. 5, pp. 725–734, 2024.

[3] N. C. Albrecht, M. Heyer, M. Wenzel, D. Langer, H. Lu, and A. Koelpin, "Long-distance heart sound detection using 122 GHz CW radar with 3D printed high-gain antennas," in *Proc. IEEE Radio Wireless Symp. (RWS)*, Jan. 2023, pp. 34–36.

[4] C. Rader, "A simple method for sampling in-phase and quadrature components," *IEEE Trans. Aerosp. Electron. Syst.*, vols. AES–20, no. 6, pp. 821–824, Nov. 1984.

[5] K. C. Ho, Y. T. Chan, and R. Inkol, "A digital quadrature demodulation system," *IEEE Trans. Aerosp. Electron. Syst.*, vol. 32, no. 4, pp. 1218–1227, Apr. 1996.

[6] M. Servin, J. A. Quiroga, and J. L. Marroquin, "General n-dimensional quadrature transform and its application to interferogram demodulation," *J. Opt. Soc. Amer. A, Opt. Image Sci.*, vol. 20, no. 5, pp. 925–934, May 2003.

[7] M. Carrick, "Design and application of a Hilbert transformer in a digital receiver," in *Proc. SDR Tech. Conf. Prod. Expo.*, 2011. [Online]. Available: https://api.semanticscholar.org/CorpusID:195808045

[8] J. Liu, F. Tong, and C. Gu, "Non-contact vital sign detection with high noise and clutter immunity based on coherent low-IF CW radar," *IEEE J. Electromagn., RF Microw. Med. Biol.*, vol. 9, no. 1, pp. 90–100, Mar. 2025.

[9] F. Tong, J. Liu, C. Li, C. Gu, and J. Mao, "A low-IF Doppler radar with asynchronous bandpass sampling for accurate measurement of displacement motions," *IEEE Trans. Microw. Theory Techn.*, vol. 71, no. 1, pp. 456–465, Jan. 2023.

[10] P. Tschapek, G. Körner, C. Carlowitz, and M. Vossiek, "Detailed analysis and modeling of phase noise and systematic phase distortions in FMCW radar systems," *IEEE J. Microw.*, vol. 2, no. 4, pp. 648–659, Oct. 2022.

[11] S. Ahmed, "Electronic microwave imaging with planar multistatic arrays," Ph.D. thesis, Fac. Eng., Alexander University of Erlangen, Erlangen, Germany, Aug. 2015.

[12] S. Kueppers, H. Cetinkaya, R. Herschel, and N. Pohl, "A compact 24 × 24 channel MIMO FMCW radar system using a substrate integrated waveguide-based reference distribution backplane," *IEEE Trans. Microw. Theory Techn.*, vol. 68, no. 6, pp. 2124–2133, Jun. 2020.

[13] J. Bott et al., "An 8 × 8 MIMO radar system utilizing cascadable transceiver MMICs with on-chip antennas at 240 GHz," *IEEE Trans. Radar Syst.*, vol. 2, pp. 805–820, 2024.

[14] L. Sigg et al., "Over-the-air synchronization for coherent digital automotive radar networks," *IEEE Trans. Radar Syst.*, vol. 2, pp. 739–751, 2024.

[15] A. Dürr et al., "High-resolution 160-GHz imaging MIMO radar using MMICs with on-chip frequency synthesizers," *IEEE Trans. Microw. Theory Techn.*, vol. 67, no. 9, pp. 3897–3907, Sep. 2019.

[16] M. Gottinger, P. Gulden, and M. Vossiek, "Coherent signal processing for loosely coupled bistatic radar," *IEEE Trans. Aerosp. Electron. Syst.*, vol. 57, no. 3, pp. 1855–1871, Jun. 2021.

[17] A. Frischen, J. Hasch, and C. Waldschmidt, "A cooperative MIMO radar network using highly integrated FMCW radar sensors," *IEEE Trans. Microw. Theory Techn.*, vol. 65, no. 4, pp. 1355–1366, Apr. 2017.

[18] C. Nguyen, *Theory, Analysis and Design of RF Interferometric Sensors*. New York, NY, USA: Springer, 2011.

[19] P. Hariharan, *Optical Interferometry*, 2nd ed., New York, NY, USA: Academic, 2003.

[20] M. C. Budge and M. P. Burt, "Range correlation effects in radars," in *Proc. Rec. IEEE Nat. Radar Conf.*, Apr. 1993, pp. 212–216.

[21] E. Bedrosian, "A product theorem for Hilbert transforms," *Proc. IEEE*, vol. 51, no. 5, pp. 868–869, 1963.

[22] J. Lawrence, *A Catalog of Special Plane Curves*. New York, NY, USA: Dover, 2013.

[23] R. Yates, *A Handbook on Curves and Their Properties*. Denver, CO, USA: J.W. Edwards, 1947.

[24] B. Tegowski, D. Langer, M. Wenzel, N. C. Albrecht, and A. Koelpin, "Near-field scattering phenomena in monostatic radar applications derived from physical optics," *IEEE Trans. Antennas Propag.*, vol. 73, no. 2, pp. 1084–1094, Feb. 2025.

[25] D. C. Liu and J. Nocedal, "On the limited memory BFGS method for large scale optimization," *Math. Program.*, vol. 45, nos. 1–3, pp. 503–528, Aug. 1989.

[26] A. Singh et al., "Data-based quadrature imbalance compensation for a CW Doppler radar system," *IEEE Trans. Microw. Theory Techn.*, vol. 61, no. 4, pp. 1718–1724, Apr. 2013.

[27] B. Tegowski and A. Koelpin, "Accuracy limitations of interferometric radar owing to the radar cross section of its antenna," *IEEE Trans. Microw. Theory Techn.*, vol. 72, no. 7, pp. 4317–4324, Jul. 2024.

[28] B. Tegowski, B. Schulz, and A. Koelpin, "Empirical study on the antenna-dependent accuracy of continuous- wave radars," in *Proc. 15th German Microw. Conf. (GeMiC)*, Mar. 2024, pp. 105–108.

Nils C. Albrecht (Graduate Student Member, IEEE) received the B.Sc. and M.Sc. degrees from Hamburg University of Technology, Hamburg, Germany, in 2018 and 2021, respectively, where he is currently pursuing the Ph.D. degree at the Institute of High-Frequency Technology.

His current research interests include radar systems for medical applications, software-defined radar, and machine learning for radar signals.

Mr. Albrecht was a recipient of the First Prize of the Radar for Noncontact Vital Sign Sensing of the IEEE International Microwave Symposium in 2021, 2022, and 2023, respectively. Additionally, he received the Science Award of the Gisela and Erwin Sick Foundation. He serves as a reviewer for IEEE TRANSACTIONS ON RADAR SYSTEMS and IEEE OPEN JOURNAL OF ENGINEERING IN MEDICINE AND BIOLOGY.

Philip Riege received the B.Sc. and M.Sc. degrees from Hamburg University of Technology, Hamburg, Germany, in 2020 and 2023, respectively.

Since 2024, he has been with the Institute of High-Frequency Technology, where he is currently a Research Assistant. His research interests include wireless, low-power communication, and radar systems.

Bartosz Tegowski was born in 1997. He received the B.Sc. and M.Sc. degrees in electrical engineering from Hamburg University of Technology, Hamburg, Germany, in 2019 and 2021, respectively, where he is currently pursuing the Ph.D. degree at the Institute of High-Frequency Technology.

His current research interests include microwave filter design, electromagnetic theory, modeling of near-field scattering, and interferometric radar systems.

Mr. Tegowski was a recipient of the Science Award of the Gisela and Erwin Sick Foundation and the First Prize from the 3D-Printed Surface-Mounted Filter Student Design Competition of the IEEE International Microwave Symposium in 2023. He received the Best Student Paper Award of the German Microwave Conference in 2024, the Young Scientist Award of the International Radar Symposium in 2025, and the Young Engineer Prize of the European Microwave Conference in 2025. He serves as a reviewer for IEEE MICROWAVE AND WIRELESS TECHNOLOGY LETTERS.

Dominik Langer (Graduate Student Member, IEEE) received the B.Sc. and M.Sc. degrees in electrical engineering from Hamburg University of Technology, Hamburg, Germany, in 2018 and 2021, respectively, where he is currently pursuing the Ph.D. degree at the Institute of High-Frequency Technology.

His current research interests include antenna design, additive manufacturing, and interferometric radar systems.

Mr. Langer was a recipient of the First Prize of the Radar for Noncontact Vital Sign Sensing of the IEEE International Microwave Symposium in 2021, 2022, and 2023, respectively. He serves as a reviewer for IEEE MICROWAVE AND WIRELESS TECHNOLOGY LETTERS.

Alexander Koelpin (Fellow, IEEE) received the Diploma degree in electrical engineering and the Ph.D. and Habilitation degrees from the University of Erlangen–Nuremberg (FAU), Erlangen, Germany, in 2005, 2010, and 2014, respectively.

From 2005 to May 2017, he was with the Institute for Electronics Engineering, FAU. From 2007 to 2010, he was a Team Leader, from 2010 to 2015, a Group Leader of Circuits, Systems, and Hardware Test, and since 2015, he has been a Leader of the Group Electronic Systems. From June 2017 to February 2020, he was a Professor and the Head of the Chair for Electronics and Sensor Systems with the Brandenburg University of Technology Cottbus–Senftenberg, Cottbus, Germany. Since March 2020, he has been with Hamburg University of Technology, Hamburg, Germany, as a Professor and the Head of the Institute of High-Frequency Technology. He has authored or co-authored more than 300 publications in his areas of interest. He serves as a reviewer for several journals and conferences. His research interests are in the areas of microwave circuits and systems, radar and wireless sensing, wireless communication systems, local positioning, and six-port technology.

Dr. Koelpin was a member of the Commission A: Electromagnetic Metrology of U.R.S.I. from 2012 to 2017. He has been an Elected Member since 2018 and has been the Vice Chair of the IEEE MTT-S/AP German Chapter Executive Board since 2020. He received the IEEE MTT-S Outstanding Young Engineer Award in 2016 and the ITG Award of the German VDE in 2017. He was the Chair of the IEEE MTT-S Technical Committee MTT-24, from 2018 to 2020. He served as the Conference Co-Chair for the IEEE Topical Conference on Wireless Sensors and Sensor Networks, the Conference Chair for the 2020 German Microwave Conference, the Technical Program Chair for IEEE Radio and Wireless Week 2021, and the General Chair for IEEE Radio and Wireless Week 2023.